JACS
JOURNAL OF THE AMERICAN CHEMICAL SOCIETY

Article

pubs.acs.org/JACS

Carrier Diffusion Lengths of over 500 nm in Lead-Free Perovskite $CH_3NH_3SnI_3$ Films

Lin Ma,[‡] Feng Hao,[‡] Constantinos C. Stoumpos, Brian T. Phelan, Michael R. Wasielewski,* and Mercouri G. Kanatzidis*

Department of Chemistry, Argonne-Northwestern Solar Energy Research (ANSER) Center, and Institute for Sustainability and Energy at Northwestern (ISEN), Northwestern University, 2145 Sheridan Road, Evanston, Illinois 60208, United States

Supporting Information

ABSTRACT: The dynamics of photoexcited lead-free perovskite films, $CH_3NH_3SnI_3$, were studied using broadband transient absorption and time-resolved fluorescence spectroscopy. Similar to its lead analogue $CH_3NH_3PbI_3$, we show that free carrier (electrons and holes) recombination is also the dominant relaxation pathway in $CH_3NH_3SnI_3$ films. The slow hot carrier relaxation time is 0.5 ps. Long carrier diffusion lengths for electrons (279 ± 88 nm) and holes (193 ± 46 nm) were obtained from fluorescence quenching measurements. We also show that SnF_2 doping in the $CH_3NH_3SnI_3$ film effectively increases the fluorescence lifetime up to 10 times and gives diffusion lengths exceeding 500 nm. These results suggest that the photophysics of $CH_3NH_3SnI_3$ perovskite are as favorable as those of $CH_3NH_3PbI_3$, demonstrating that it is a promising nontoxic lead-free replacement for lead iodide perovskite-based solar cells.

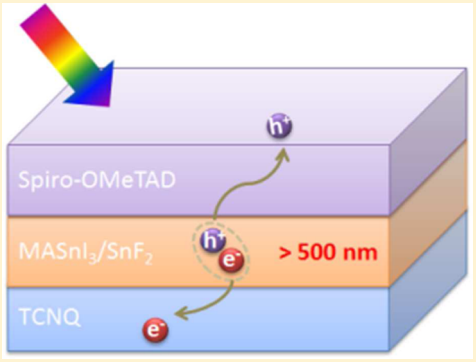

INTRODUCTION

Organic−inorganic metal halide perovskite solar cells (PSCs) have recently attracted tremendous attention due to the the impressive increase in their efficiency witnessed in the past few years.[1−3] The power conversion efficiency (PCE) of PSCs has leapt from the initial 3.8% in 2009[4] to 22.1% in 2015.[5] The organic−inorganic hybrid nature of perovskite materials promises both the superior carrier mobility of inorganic semiconductors and the processability of organic materials.[6] To date, mainstream PSC development has focused on methylammonium lead iodide, $CH_3NH_3PbI_3$ and mixed halide perovskite blends, $CH_3NH_3PbI_{3-x}Br_x$ or $CH_3NH_3PbI_{3-x}Cl_x$, featuring high absorption coefficients, long carrier diffusion lengths,[7,8] and high charge carrier mobilities.[9] Carrier recombination occurs on a time scale of hundreds of nanoseconds, resulting in long carrier diffusion lengths ranging between 100 nm for the pristine material and 1000 nm for the I/Cl blend.[7,8] Most recently, a carrier diffusion length as long as 175 μm was reported in single crystals of the $CH_3NH_3PbI_3$ perovskite.[10]

The large-scale use of soluble lead-based materials, however, raises concern about their potential toxicity,[11,12] even though the lead content in each single solar cell is very small. The use of lead-containing substances in electronics devices has been severely restricted by the European Union and other countries, thus calling for the development of a nontoxic replacement for lead perovskite without severely affecting the photovoltaic performance. The fabrication of solar cells with lead-free, tin iodide perovskite ($CH_3NH_3SnI_3$ or $CsSnI_3$) has been reported, albeit with low efficiency.[13−15] Featuring a narrower optical bandgap of 1.3 eV,[13] compared to 1.55 eV[16] for $CH_3NH_3PbI_3$, the tin iodide perovskite can potentially provide better photovoltaic performance owing to its broader solar spectrum absorption. Unfortunately, the device performance of Sn-based perovskites shows a wide variation, with a large fraction of them being short-circuited and others showing a broad distribution of reported efficiencies.[15,17,18] This is mainly a result of the rapid oxidation of Sn^{2+} to Sn^{4+}, which occurs when the devices are exposed in air, and until now this process has not been well understood or controlled. Although research focused on tin iodide perovskite raises hopes toward lead-free PSCs, the intrinsic properties of the devices need to be better understood, particularly the photoexcited-state properties. Understanding the excited-state dynamics in perovskites is imperative for further optimization of PSCs, as charge generation and recombination processes play important roles in dictating optoelectronic performance.

In this work, we present an extensive spectroscopic study of the excited-state dynamics in $CH_3NH_3SnI_3$ perovskite films using broadband (visible and near-infrared, Vis-NIR) transient absorption (TA) and time-resolved fluorescence (TRF) spectroscopy. The decay kinetics of TA spectra and TRF emission follow a second-order recombination model, thus confirming that the predominant relaxation pathway in $CH_3NH_3SnI_3$ is carrier recombination.[19] We also observe the hot carrier relaxation via the excitation wavelength-dependent TA measurements. By measuring the fluorescence decay with

Received: September 2, 2016
Published: October 17, 2016

DOI: 10.1021/jacs.6b09257
J. Am. Chem. Soc. 2016, 138, 14750−14755

additional quenching layers for electrons (TCNQ, 7,7,8,8-tetracyanoquinodimethane) or holes (Spiro-OMeTAD, 2,2′,7,7′-tetrakis(*N*,*N*-di-*p*-methoxyphenylamine)-9,9′-spirobifluorene), we obtain long carrier diffusion lengths (279 ± 88 nm for electrons and 193 ± 46 nm for holes) in pristine $CH_3NH_3SnI_3$ films, twice as large as the initial reported values in $CH_3NH_3PbI_3$ films.[7,8] Further doping by adding SnF_2 to the precursor solution results in 10 times longer fluorescence lifetime and >500 nm carrier diffusion length, which indicates the tin iodide PSCs may achieve a better performance than lead iodide PSCs with further device optimization.

EXPERIMENTAL SECTION

Materials. Unless stated otherwise, all materials were purchased from Sigma-Aldrich and used as received. Spiro-OMeTAD and TCNQ were purchased from Feiming Chemical and Merck KGaA. CH_3NH_3I and SnI_2 were synthesized and purified according to our previously reported procedure.[33] The $CH_3NH_3SnI_3$ film on pre-cleaned soda-lime glass substrate were prepared by spin-coating an anhydrous dimethylformamide (DMF) solution containing an equivalent molar ratio of CH_3NH_3I and SnI_2 precursors at 5000 rpm for 30 s. The films were annealed on a hot plate at 70 °C for 30 min. The obtained films were sealed along the edges with a thermal plastic film (Surlyn film, 30 μm) to prevent any degradation due to air and moisture exposure. All the fabrication and packaging procedures were carried out in the glovebox filled with nitrogen atmosphere. The thicknesses of as-fabricated $CH_3NH_3SnI_3$ films were measured by cross-sectional scanning electron microscopy (SEM, S4800, Hitachi) to be 335 ± 75 nm (obtained by measuring five films from the same batch).

Vis-NIR femtosecond transient absorption (fsTA) spectroscopy was performed using an instrument previously described.[20] Briefly, the approximately 120 fs, 1 kHz output of a commercial Ti:sapphire oscillator/amplifier (Tsunami/Spitfire, Spectra-Physics) was split to seed and pump a laboratory-constructed optical parametric amplifier used to generate the 650 nm excitation ("pump") beam, and to generate a femtosecond continuum probe, by using either a sapphire crystal for the visible range or a proprietary crystal for the NIR spectral region (Ultrafast Systems, LLC). Transient spectra were collected by using customized commercial detectors (Helios, Ultrafast Systems, LLC). The polarization of the pump is fixed at the magic angle (54.7°) with respect to the probe polarization.

Low-fluence fsTA experiments were performed using a high repetition rate instrument. The fundamental output (1040 nm, 4.5 W, 350 fs) of a commercial direct diode-pumped 100 kHz amplifier (Spirit 1040-4, Spectra Physics) was divided into two beam paths with a beam splitter. White light continuum probe pulses (480−900 nm) were created by focusing the smaller fraction (0.50 W) to a ~40 μm spot size in a 5 mm thick undoped yttrium aluminum garnet crystal. The larger fraction (4.0 W) was used to drive a non-collinear optical parametric amplifier (Spirit-NOPA-3H, Light Conversion) to create the 600 nm pump pulses. After passing through the sample, the continuum probe was spectrally dispersed inside a modified SPEX 270m monochromator equipped with a 600 grooves/mm grating, and collected by a CMOS linear image sensor (S10112-512Q, Hamamatsu). Signal differencing was achieved by chopping the pump beam prior to the sample position at 476 Hz. The average total exposure time per data point in the experiments is 10 s, which results in a typical baseline noise of $\Delta A \approx 5 \times 10^{-6}$. The instrument response function (IRF) is around 150 fs.

TA spectra were analyzed via singular value decomposition (SVD) using lab-written Matlab programs. SVD deconvolutes the two-dimensional spectra to produce an orthonormal set of basis spectra which describe the wavelength dependence of the species and a corresponding set of orthogonal vectors which describes the time-dependent amplitude of the basis spectra.[21] A species-associated[22] second-order kinetic model (eqs 1 and 2 in the main text) was fit to a linear combination of the time-dependent amplitude vectors and the same linear combination of basis spectra was used to construct the spectra for the chemical species.

Time-resolved fluorescence data were collected at room temperature using a streak camera system (Hamamatsu C4334 Streakscope). The IRF is about 30 ps. After deconvolution fitting, the temporal resolution is ~10 ps. 600 nm laser pulses were utilized as the excitation source, which were generated by the same high repetition rate (100 kHz) ultrafast laser system mentioned above for the low-fluence TA instrument.

RESULTS AND DISCUSSION

Broadband Transient Absorption Spectroscopy. In this study, we first measured the steady-state absorption and fluorescence spectra of the pristine $CH_3NH_3SnI_3$ films. The steady-state absorption spectrum was recorded with an integrating sphere to eliminate the influence due to scattering. The spectrum covers the entire visible range up to 950 nm, showing an absorption coefficient ~2.0×10^4 cm^{-1} (Supporting Information, Figure S1), consistent with the previous report.[14] The absorption coefficient for $CH_3NH_3SnI_3$ is 1 order of magnitude lower than that of the benchmark $CH_3NH_3PbI_3$.[23] The fluorescence spectrum is centered at ~950 nm using 450 nm excitation (Figure S1), consistent with the optical band gap of $CH_3NH_3SnI_3$ perovskite (1.30 eV). The powder X-ray diffraction patterns and UV−vis absorption spectra of the perovskite films before and after the TA spectroscopy are shown in Figure S2. Both the XRD and absorption spectra confirm the pure phase of $CH_3NH_3SnI_3$.

We then carried out Vis-NIR fsTA spectroscopy using a 1 kHz laser system described previously.[24] Figure 1a shows the

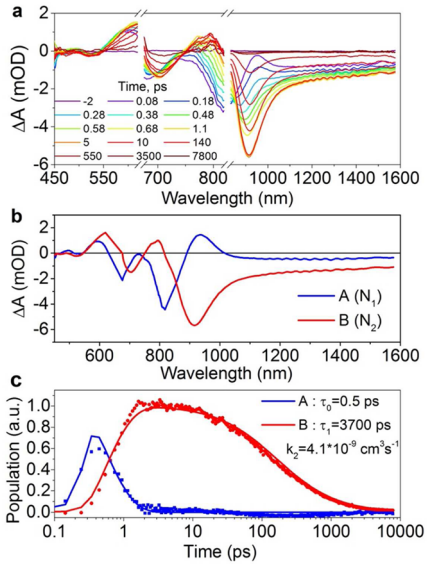

Figure 1. (a) Transient absorption spectra in the visible and NIR range under excitation at 650 nm at room temperature. The scattering from the pump (650 nm) and fundamental beam (830 nm) was removed for clarity. (b) Species-associated spectra and (c) kinetics reconstructed from the SVD global fit.

Vis-NIR TA spectra of a $CH_3NH_3SnI_3$ film using a 420−1600 nm probe pulse. There are four main features in the TA spectra: (i) a pronounced ground state bleaching (GSB) at 920 nm (1.35 eV), which is close to the optical bandgap 1.30 eV;[13] (ii) a relatively weak bleaching feature at 710 nm; (iii) a photo-induced absorption (PIA) band at 800 nm; and (iv) a PIA band at 630 nm. The 920 nm GSB band is accompanied by a flat

DOI: 10.1021/jacs.6b09257
J. Am. Chem. Soc. 2016, 138, 14750−14755

negative TA feature in the NIR region (1100−1600 nm) which is assigned to the carrier trap states on the film surface.[25] Moreover, there is a pronounced spectral red shift within the first 1 ps over the entire wavelength range probed.

The recovery of the TA signal (GSB and PIA) is attributed to the recombination of photogenerated free carriers rather than excitons, since a second-order recombination model is needed to obtain a satisfactory kinetic fit. The presence of free carriers at room temperature suggests a very low exciton binding energy in $CH_3NH_3SnI_3$, which agrees well with electronic structure calculations (for the nearly isostructural perovskite α-$CsSnI_3$,[26] in lieu of related data for α-$CH_3NH_3SnI_3$), which suggests a screened exciton binding energy <1 meV. The presence of free-carriers is confirmed further by the intensity-dependent fluorescence lifetime measurements discussed below.

Kinetic analyses of the TA data sets were performed using SVD[27] followed by global fitting to a second-order kinetic rate model (eqs 1 and 2):

$$\frac{dN_1}{dt} = -\frac{N_1}{\tau_0} \quad (1)$$

$$\frac{dN_2}{dt} = \frac{N_1}{\tau_0} - k_1N_2 - k_2N_2^2 \quad (2)$$

where N_1 is the population of initially generated "hot" carriers, τ_0 is the hot carrier relaxation time, N_2 is the population of carriers relaxed to the band edge, k_1 is the first-order rate constant for single carrier trapping (trap state-mediated recombination) and k_2 is the second-order rate constant for free carrier (electrons and holes) recombination,[28] which depends on the initial carrier density N_0. The species-associated spectra and kinetics reconstructed from the global fits are presented in Figure 1b,c. The SVD global fit yields τ_0 = 0.5 ps which is similar to the hot carrier cooling time in $CH_3NH_3PbI_3$ films (Figure S4b); the trap-state-mediated recombination time $\tau_1 = 1/k_1$ = 3.7 ns; the second-order rate constant k_2 = 4.1 × 10^{-9} cm^3 s^{-1}, about twice larger than that for $CH_3NH_3PbI_3$ films (2.3 × 10^{-9} cm^3 s^{-1}).[29]

The origin of the spectral red shift in Figure 1a was investigated further by varying the excitation wavelength from 430 to 900 nm (Figure S5). To rule out the band-filling effect induced by a high carrier density,[29] we performed the TA measurements in the visible probe range with a low-fluence high-repetition rate (100 kHz) laser system (see Supporting Information), which allows us to use 100 times lower intensity to get a similar signal-to-noise ratio as the conventional 1 kHz system. Figure 2 shows the pseudo-color (ΔA) representation of the TA spectra as a function of probe wavelength and delay time between pump and probe. The white dashed lines plotted in the 710 nm GSB region are a guide to the eye. A clear trend can be observed, indicating that with increasing excitation wavelength, i.e., decreasing excitation photon energy, the spectral red shift becomes less obvious; in particular, when the excitation photon energy approaches the optical band gap (λ_{exc} = 900 nm), this red shift disappears. There is an additional pronounced PIA band at 730 nm due to hot carrier absorption when the excitation photon energy is well above band gap (e.g., λ_{exc} = 430 and 600 nm). This excitation energy dependence of the TA spectra is a strong evidence for the hot carrier relaxation model we used above for the global analyses of the TA spectra. Furthermore, we found that the relaxation time τ_0 is independent of excitation intensity (Figure S3), which reveals

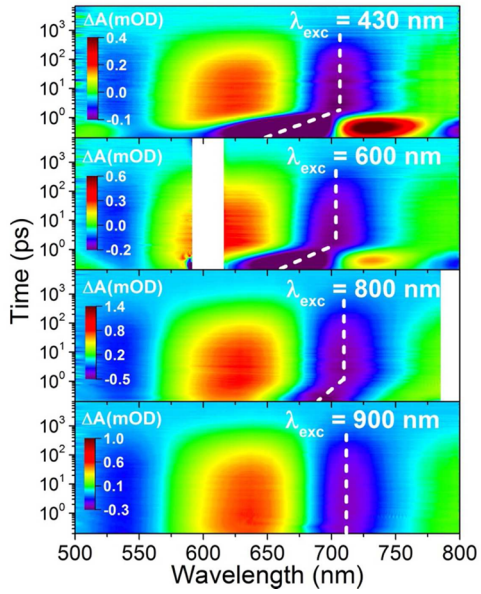

Figure 2. Excitation energy-dependent transient absorption spectra of a $CH_3NH_3SnI_3$ perovskite film. The white dashed lines are used as guides to the eye. All measurements were performed at room temperature.

that the observed hot carrier cooling is mainly due to electron−phonon interactions rather than electron−electron scattering.

For comparison, the excitation energy-dependent TA spectra of a $CH_3NH_3PbI_3$ perovskite film were also studied (Figure S4), which showed good agreement with previous reports.[28,30] It is noteworthy that the spectral red shift is less obvious in $CH_3NH_3PbI_3$ than that in $CH_3NH_3SnI_3$ films. The reason seems to be that the carrier cooling and bandgap renormalization compensate each other in $CH_3NH_3PbI_3$.[30] Similarly, we also see a positive PIA band due to bandgap renormalization located at the lower energy side (935 nm, 1.33 eV) of the main GSB band (920 nm, 1.35 eV) based on the SVD fit in Figure 1b. By using these two values, we can estimate the bandgap renormalization energy ΔE. The bandgap renormalization energy ΔE = 0.02 eV in $CH_3NH_3SnI_3$ is lower than that in $CH_3NH_3PbI_3$ (ΔE = 0.05 eV).[30] Therefore, the bandgap renormalization observed after photoexcitation is less pronounced in $CH_3NH_3SnI_3$ film.

Time-Resolved Fluorescence Spectroscopy. The TRF emission decays of the $CH_3NH_3SnI_3$ films show a strong dependence on excitation intensity because it is dominated by second-order free carrier (electron−hole) recombination (Figure 3). The kinetic fits obtained at the 950 nm emission maximum based on the second-order kinetic model (eq 3) are summarized in Table 1.

$$\frac{dN_2}{dt} = -k_1N_2 - k_2N_2^2 \quad (3)$$

The fluorescence decay at the lowest carrier concentration (N_0 = 5.1 × 10^{15} cm^{-3}) shows the longest lifetime, which can be well fit with a single exponential decay indicating that at low excitation intensity the excited state decay is dominated by trap state mediated emission (a first-order process).[31] With increasing carrier density, a second-order rate constant k_2 is needed to fit the data. The fitting for fluorescence kinetics at carrier concentrations between 2.2 × 10^{16} and 1.5 × 10^{17} cm^{-3} results in a similar $k_2 \approx 3.8 \times 10^{-9}$ cm^3 s^{-1} (Table 1). When the

DOI: 10.1021/jacs.6b09257
J. Am. Chem. Soc. 2016, 138, 14750−14755

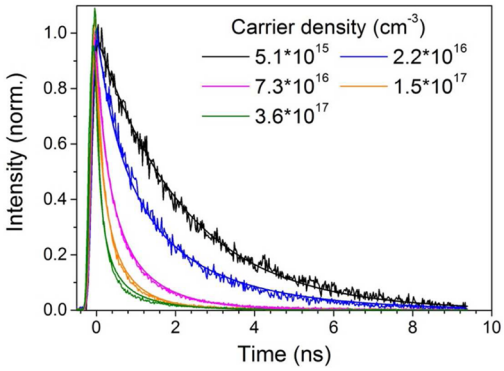

Figure 3. Time-resolved fluorescence kinetics of 950 nm at various excitation intensities under 600 nm excitation. Each trace is normalized to its maximum intensity.

Table 1. Second-Order Charge Recombination Kinetics

carrier density N_0 (cm^{-3})	τ_1 ($1/k_1$, ns)	k_2 ($cm^3\ s^{-1}$)
5.1×10^{15}	2.24 ± 0.02	–
2.2×10^{16}	2.61 ± 0.02	$(3.97 \pm 0.02) \times 10^{-9}$
7.3×10^{16}	1.20 ± 0.02	$(3.66 \pm 0.03) \times 10^{-9}$
1.5×10^{17}	0.89 ± 0.03	$(3.85 \pm 0.07) \times 10^{-9}$
3.6×10^{17}	1.20 ± 0.07	$(5.33 \pm 0.30) \times 10^{-9}$

carrier density is further increased >3.6×10^{17} cm^{-3}, k_2 becomes larger (5.3×10^{-9} $cm^3\ s^{-1}$), which can be attributed to an additional contribution from Auger recombination (third-order process) at high excitation fluence.[28]

Electron and Hole Diffusion Lengths for $CH_3NH_3SnI_3$ Film. To estimate the electron and hole diffusion lengths, we performed fluorescence quenching measurements by depositing additional quencher layers for electrons (TCNQ) and holes (Spiro-OMeTAD) on top of the $CH_3NH_3SnI_3$ films. To ensure the reliability of results, we always prepared fresh spin coated films (under the same conditions) before each measurement. For diffusion length measurements, we typically prepare three films together, one as pristine film to get the carrier lifetime, one deposited with TCNQ layer to get the electron diffusion length, and one deposited with Spiro-OMeTAD layer on top to get the hole diffusion length. The representative cross-sectional SEM images of the perovskite film with quenching layer on top are shown in Figure S6 with a perovskite layer thickness of ~330 nm and a quenching layer of ~50 nm for Spiro-OMeTAD and 40 nm for TCNQ layer. The measured fluorescence decays are shown in Figure 4a. The fluorescence decays of the $CH_3NH_3SnI_3$/TCNQ and $CH_3NH_3SnI_3$/Spiro-OMeTAD films are then fit according to a one-dimensional diffusion model (eq 4),

$$\frac{\partial N(x,t)}{\partial t} = D\frac{\partial^2 N(x,t)}{\partial x^2} - k_{\text{eff}}N(x,t) \quad (4)$$

$$k_{\text{eff}} = -\frac{1}{N_2}\frac{dN_2}{dt} = k_1 + k_2 N_2 \quad (5)$$

where D is the diffusion coefficient and k_{eff} is the "effective first-order" recombination rate constant in the pristine $CH_3NH_3SnI_3$ film, defined according to eq 5.[32] From the fitting we obtain the electron and hole diffusion coefficients D_e = 1.28 ± 0.73 $cm^2\ s^{-1}$ and D_h = 0.59 ± 0.27 $cm^2\ s^{-1}$, respectively. These values are about 30 times larger than the diffusion constants reported in a $CH_3NH_3PbI_3$ film (D_e = 0.036 $cm^2\ s^{-1}$ and D_h = 0.022 $cm^2\ s^{-1}$).[7] The present results are consistent with our previous studies of the bulk perovskites using Hall-effect measurements, showing a high electron mobility $\mu_e \approx 60$ $cm^2\ V^{-1}\ s^{-1}$ for $CH_3NH_3PbI_3$ and very high mobilities $\mu_e \approx 2000$ $cm^2\ V^{-1}\ s^{-1}$ and $\mu_h \approx 300$ $cm^2\ V^{-1}\ s^{-1}$ for electrons and holes, respectively, in $CH_3NH_3SnI_3$.[33] These differences originate directly from the electronic band structure of the two perovskites,[34,35] in which the calculations unanimously suggest a much larger bandwidth for both the valence and conduction bands of the Sn perovskite. The greater bandwidth suggests lower effective masses for the charge carriers, and by extension, higher electron mobility. Based on the measured diffusion coefficients, we further calculated the electron and hole diffusion lengths (L_D) to be L_D^e = 279 ± 88 nm and L_D^h = 193 ± 46 nm, where $L_D = \sqrt{D\tau} = \sqrt{D/k_{\text{eff}}}$. The uncertainty of measured diffusion lengths is mainly due to the accuracy of film thickness. Fluorescence quenching measurements were repeated for five independent batches of films grown under the same experimental conditions (Figure S7), showing a reasonable spread of carrier diffusion lengths (Table S2): L_D^e ranges from 160 to 372 nm, and L_D^h varies from 118 to 306 nm. It is worth mentioning that, owing to the superior carrier mobilities in $CH_3NH_3SnI_3$, although the carrier lifetime in $CH_3NH_3SnI_3$ is much shorter than that of $CH_3NH_3PbI_3$ films, the carrier diffusion lengths are still about twice as large as the initial reported values in $CH_3NH_3PbI_3$ films (L_D^e = 130 nm, L_D^h = 110 nm).[7,8] It is important to point out that the obtained carrier diffusion length in our work is significant longer than the initial reported value (about 30 nm from the time-resolved optical pump THz probe spectroscopy) along with a 200 ps PL lifetime.[15] This could be due to the difference in film quality or morphology between the two films. We made another important comparison with the $CH_3NH_3SnI_3$ films made with commercial SnI_2 source (99.999% trace metals basis, Sigma-

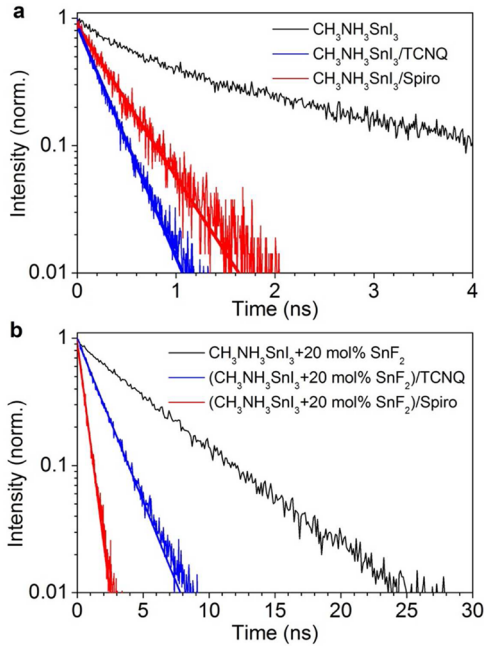

Figure 4. Time-resolved fluorescence kinetics at 950 nm for (a) $CH_3NH_3SnI_3$ and (b) $CH_3NH_3SnI_3$ + 20 mol % SnF_2 films of pristine (black), with electron (TCNQ, blue) or hole (Spiro, red) quencher layer under excitation at 600 nm. The solid lines are the fittings according to the diffusion model described in the text.

DOI: 10.1021/jacs.6b09257
J. Am. Chem. Soc. 2016, 138, 14750−14755

Aldrich). Figure S8 shows the corresponding fluorescence decays of the pristine $CH_3NH_3SnI_3$ film, $CH_3NH_3SnI_3$/TCNQ and $CH_3NH_3SnI_3$/Spiro-OMeTAD films. A significant decrease (up to 30 times of magnitude) of the fluorescence lifetimes in all the films was observed. This highlights that the carrier diffusion length in the tin perovskite is highly dependent on the material quality, and the vacuum purification process for the SnI_2 source material is necessary to ensure higher carrier diffusion lengths in the final perovskite films.

Electron and Hole Diffusion Lengths for SnF_2-Doped $CH_3NH_3SnI_3$ Film. Further enhancements on fluorescence lifetime and carrier diffusion lengths were observed in the $CH_3NH_3SnI_3$ films by adding 20 mol% of SnF_2 into the precursor solution. The addition of SnF_2 was reported to be critical in ensuring efficient photovoltaic effects in the lead-free PSCs, such as $CH_3NH_3SnI_3$,[36] $HC(NH_2)_2SnI_3$,[37] as well as its inorganic analogue, $CsSnI_3$.[15,38] The reason is not clearly understood but theoretical studies have suggested that the presence of SnF_2 in the lead-free perovskite increases the Sn chemical potential, which further increases the formation energy of the Sn vacancies, resulting in a reduction of background carrier density and a decreased concentration of defects.[15] A typical SEM image, XRD, and UV−vis absorbance spectra of the $CH_3NH_3SnI_3$ films with 20 mol% SnF_2 are shown in Figures S9 and S10. It should be noted that we did not observe any peak of SnF_2 or SnI_2 instead of the main (001) and (002) peaks for $CH_3NH_3SnI_3$ with a homogeneous morphology. This is significantly different from the Cl^- effect in the $CH_3NH_3PbI_3$ films, in which a $CH_3NH_3PbCl_3$ secondary phase is usually produced to enhance the film properties such as the diffusion length.[7,8] In our case we expect no real "doping" effect from F^- ions. The SnF_2 seems to act as an inhibitor of Sn^{2+} oxidation in the precursor solution which is sufficient to produce a relatively undoped (Sn^{4+}-free) film with lower defect concentration.

Time-resolved fluorescence were measured for four independent batches of ($CH_3NH_3SnI_3$ + 20 mol% SnF_2) films grown under the same experimental conditions (Figure S11), showing ∼10 times longer fluorescence lifetimes than the pristine $CH_3NH_3SnI_3$ films. It indicates that the addition of SnF_2 also helps to reduce the defect concentration in $CH_3NH_3SnI_3$ films. Carrier diffusion lengths in the ($CH_3NH_3SnI_3$ + 20 mol% SnF_2) films were estimated by the same fluorescence quenching method mentioned above (Figure S12), showing L_D^e = 258 ± 58 nm and L_D^h = 549 ± 124 nm. These results indicate that there is still great potential for improving the performance of $CH_3NH_3SnI_3$ films based solar cells. Control measurements were performed to validate the accuracy of the obtained long fluorescence lifetimes by reversing the measurement geometry. The Spiro-OMeTAD layer was intentionally deposited underneath the perovskite layer. Figure S13 shows the representative fluorescence decays for the pristine $CH_3NH_3SnI_3/SnF_2$, $CH_3NH_3SnI_3/SnF_2$/Spiro-OMeTAD, and also the Spiro-OMeTAD/$CH_3NH_3SnI_3/SnF_2$ films. The latter two films showed comparable quenching lifetimes irrespective of the order of the perovskite and quenching layer, indicating the effect of the perovskite film's uniformity on the fluoresence lifetime is negligible in this study.

The long carrier diffusion lengths should make it possible to fabricate planar structure device without a mesoporous electron-selective layer. Preliminary photovoltaic result on the planar device with a configuration of FTO/blocking TiO_2 layer/$CH_3NH_3SnI_3$:SnF_2/PTAA/Au was shown in Figure S14a. A short-circuit photocurrent density of 3.32 mA cm^{-2} and an open-circuit voltage of 234 mV were achieved, along with a fill factor of 40.7%. To the authors' knowledge, this is the first report on the planar heterojunction architecture solar cells with the lead-free $CH_3NH_3SnI_3$ perovskite and should be noted that the perovskite film quality and thickness is not optimized in this study. These poor photovoltaic parameters can be traced back to the high carrier recombination rate at the interface and a lower absorption coefficient of the $CH_3NH_3SnI_3$ perovskites. The deficient light harvesting can be confirming by the incident photon conversion efficiency curve (Figure S14b) with a low absorption plateau of 14.3% and the poor absorption near the optical band gap of the perovskite. To move forward, efforts should focus on improved deposition methods that enhance the film quality and film thickness, following the judicious choice of mixed halide stoichiometry to increase the carrier lifetime. The energy levels of the interface layers between perovskite and electron- and hole-selective layer should also be optimized to further push the PCE.

CONCLUSIONS

In summary, excited-state relaxation in $CH_3NH_3SnI_3$ films is dominated by free carrier recombination similar to $CH_3NH_3PbI_3$ perovskite films. The slow hot carrier relaxation (0.5 ps) indicates that hot carrier extraction may further improve PSC efficiencies. The long carrier (electron/hole) diffusion lengths, especially after SnF_2 doping, enable the realization of the first planar heterojunction device with moderate photovoltaic response. Further performance enhancement requires better perovskite film morphology and thickness control as well as judicious perovskite component modification. This study also indicates that PSCs based on $CH_3NH_3SnI_3$ may ultimately exhibit a better performance than the $CH_3NH_3PbI_3$-based PSCs in a properly designed device.

ASSOCIATED CONTENT

Supporting Information

The Supporting Information is available free of charge on the ACS Publications website at DOI: 10.1021/jacs.6b09257.

Detailed experimental procedures, Figures S1−10, and Table S1 (PDF)

AUTHOR INFORMATION

Corresponding Authors

*m-wasielewski@northwestern.edu

*m-kanatzidis@northwestern.edu

Author Contributions

‡L.M. and F.H. contributed equally to this work.

Notes

The authors declare no competing financial interest.

ACKNOWLEDGMENTS

This research was supported as part of the ANSER Center, an Energy Frontier Research Center funded by the U.S. Department of Energy, Office of Science, Office of Basic Energy Sciences (award no. DE-SC0001059), and ISEN at Northwestern University.

REFERENCES

(1) Lotsch, B. V. *Angew. Chem., Int. Ed.* **2014**, *53*, 635.

(2) Gao, P.; Gratzel, M.; Nazeeruddin, M. K. *Energy Environ. Sci.* **2014**, *7*, 2448.

DOI: 10.1021/jacs.6b09257
J. Am. Chem. Soc. 2016, 138, 14750−14755

(3) Stoumpos, C. C.; Kanatzidis, M. G. *Acc. Chem. Res.* **2015**, *48*, 2791.
(4) Kojima, A.; Teshima, K.; Shirai, Y.; Miyasaka, T. *J. Am. Chem. Soc.* **2009**, *131*, 6050.
(5) National Renewable Energy Laboratory. Best Research-Cell Efficiencies chart, www.nrel.gov/ncpv/images/efficiency_chart.jpg.
(6) Kagan, C. R.; Mitzi, D. B.; Dimitrakopoulos, C. D. *Science* **1999**, *286*, 945.
(7) Xing, G.; Mathews, N.; Sun, S.; Lim, S. S.; Lam, Y. M.; Gratzel, M.; Mhaisalkar, S.; Sum, T. C. *Science* **2013**, *342*, 344.
(8) Stranks, S. D.; Eperon, G. E.; Grancini, G.; Menelaou, C.; Alcocer, M. J. P.; Leijtens, T.; Herz, L. M.; Petrozza, A.; Snaith, H. J. *Science* **2013**, *342*, 341.
(9) Gratzel, M. *Nat. Mater.* **2014**, *13*, 838.
(10) Dong, Q.; Fang, Y.; Shao, Y.; Mulligan, P.; Qiu, J.; Cao, L.; Huang, J. *Science* **2015**, *347*, 967.
(11) Hailegnaw, B.; Kirmayer, S.; Edri, E.; Hodes, G.; Cahen, D. *J. Phys. Chem. Lett.* **2015**, *6*, 1543.
(12) Fabini, D. *J. Phys. Chem. Lett.* **2015**, *6*, 3546.
(13) Hao, F.; Stoumpos, C. C.; Cao, D. H.; Chang, R. P. H.; Kanatzidis, M. G. *Nat. Photonics* **2014**, *8*, 489.
(14) Noel, N. K.; Stranks, S. D.; Abate, A.; Wehrenfennig, C.; Guarnera, S.; Haghighirad, A.-A.; Sadhanala, A.; Eperon, G. E.; Pathak, S. K.; Johnston, M. B.; Petrozza, A.; Herz, L. M.; Snaith, H. J. *Energy Environ. Sci.* **2014**, *7*, 3061.
(15) Kumar, M. H.; Dharani, S.; Leong, W. L.; Boix, P. P.; Prabhakar, R. R.; Baikie, T.; Shi, C.; Ding, H.; Ramesh, R.; Asta, M.; Graetzel, M.; Mhaisalkar, S. G.; Mathews, N. *Adv. Mater.* **2014**, *26*, 7122.
(16) Baikie, T.; Fang, Y.; Kadro, J. M.; Schreyer, M.; Wei, F.; Mhaisalkar, S. G.; Graetzel, M.; White, T. J. *J. Mater. Chem. A* **2013**, *1*, 5628.
(17) Zuo, F.; Williams, S. T.; Liang, P.-W.; Chueh, C.-C.; Liao, C.-Y.; Jen, A. K. Y. *Adv. Mater.* **2014**, *26*, 6454.
(18) Ogomi, Y.; Morita, A.; Tsukamoto, S.; Saitho, T.; Fujikawa, N.; Shen, Q.; Toyoda, T.; Yoshino, K.; Pandey, S. S.; Ma, T.; Hayase, S. *J. Phys. Chem. Lett.* **2014**, *5*, 1004.
(19) Yamada, Y.; Nakamura, T.; Endo, M.; Wakamiya, A.; Kanemitsu, Y. *J. Am. Chem. Soc.* **2014**, *136*, 11610.
(20) Young, R. M.; Dyar, S. M.; Barnes, J. C.; Juricek, M.; Stoddart, J. F.; Co, D. T.; Wasielewski, M. R. *J. Phys. Chem. A* **2013**, *117*, 12438.
(21) Henry, E. R.; Hofrichter, J. *Methods Enzymol.* **1992**, *210*, 129.
(22) Zamis, T. M.; Parkhurst, L. J.; Gallup, G. A. *Comput. Chem.* **1989**, *13*, 165.
(23) Green, M. A.; Ho-Baillie, A.; Snaith, H. J. *Nat. Photonics* **2014**, *8*, 506.
(24) Young, R. M.; Dyar, S. M.; Barnes, J. C.; Juríček, M.; Stoddart, J. F.; Co, D. T.; Wasielewski, M. R. *J. Phys. Chem. A* **2013**, *117*, 12438.
(25) Wu, X.; Trinh, M. T.; Niesner, D.; Zhu, H.; Norman, Z.; Owen, J. S.; Yaffe, O.; Kudisch, B. J.; Zhu, X. Y. *J. Am. Chem. Soc.* **2015**, *137*, 2089.
(26) Huang, L.-y.; Lambrecht, W. R. L. *Phys. Rev. B: Condens. Matter Mater. Phys.* **2013**, *88*, 165203.
(27) Henry, E. R.; Hofrichter, J. *Methods Enzymol.* **1992**, *210*, 129.
(28) Trinh, M. T.; Wu, X.; Niesner, D.; Zhu, X. Y. *J. Mater. Chem. A* **2015**, *3*, 9285.
(29) Manser, J. S.; Kamat, P. V. *Nat. Photonics* **2014**, *8*, 737.
(30) Price, M. B.; Butkus, J.; Jellicoe, T. C.; Sadhanala, A.; Briane, A.; Halpert, J. E.; Broch, K.; Hodgkiss, J. M.; Friend, R. H.; Deschler, F. *Nat. Commun.* **2015**, *6*, 8420.
(31) Stranks, S. D.; Burlakov, V. M.; Leijtens, T.; Ball, J. M.; Goriely, A.; Snaith, H. J. *Phys. Rev. Appl.* **2014**, *2*, 034007.
(32) La-o-vorakiat, C.; Salim, T.; Kadro, J.; Khuc, M. T.; Haselsberger, R.; Cheng, L.; Xia, H.; Gurzadyan, G. G.; Su, H.; Lam, Y. M.; Marcus, R. A.; Michel-Beyerle, M. E.; Chia, E. E. *Nat. Commun.* **2015**, *6*, 7903.
(33) Stoumpos, C. C.; Malliakas, C. D.; Kanatzidis, M. G. *Inorg. Chem.* **2013**, *52*, 9019.
(34) Im, J.; Stoumpos, C. C.; Jin, H.; Freeman, A. J.; Kanatzidis, M. G. *J. Phys. Chem. Lett.* **2015**, *6*, 3503.
(35) Umari, P.; Mosconi, E.; De Angelis, F. *Sci. Rep.* **2014**, *4*, 4467.
(36) Hao, F.; Stoumpos, C. C.; Guo, P.; Zhou, N.; Marks, T. J.; Chang, R. P. H.; Kanatzidis, M. G. *J. Am. Chem. Soc.* **2015**, *137*, 11445.
(37) Koh, T. M.; Krishnamoorthy, T.; Yantara, N.; Shi, C.; Leong, W. L.; Boix, P. P.; Grimsdale, A. C.; Mhaisalkar, S. G.; Mathews, N. *J. Mater. Chem. A* **2015**, *3*, 14996.
(38) Chung, I.; Lee, B.; He, J.; Chang, R. P. H.; Kanatzidis, M. G. *Nature* **2012**, *485*, 486.

DOI: 10.1021/jacs.6b09257
J. Am. Chem. Soc. 2016, 138, 14750−14755